Yielding of Hard-Sphere Glasses during Start-Up Shear

N. Koumakis,[1] M. Laurati,[2] S. U. Egelhaaf,[2] J. F. Brady,[3] and G. Petekidis[1,*]

[1]*FORTH/IESL and Department of Materials Science and Technology, University of Crete, 71110, Heraklion, Greece*
[2]*Condensed Matter Physics Laboratory, Heinrich-Heine University, Universitätsstrasse 1, 40225 Düsseldorf, Germany*
[3]*Division of Chemistry and Chemical Engineering, California Institute of Technology, Pasadena, California 91125, USA*

(Received 20 December 2011; published 2 March 2012)

Concentrated hard-sphere suspensions and glasses are investigated with rheometry, confocal microscopy, and Brownian dynamics simulations during start-up shear, providing a link between microstructure, dynamics, and rheology. The microstructural anisotropy is manifested in the extension axis where the maximum of the pair-distribution function exhibits a minimum at the stress overshoot. The interplay between Brownian relaxation and shear advection as well as the available free volume determine the structural anisotropy and the magnitude of the stress overshoot. Shear-induced cage deformation induces local constriction, reducing in-cage diffusion. Finally, a superdiffusive response at the steady state, with a minimum of the time-dependent effective diffusivity, reflects a continuous cage breakup and reformation.

DOI: 10.1103/PhysRevLett.108.098303 PACS numbers: 82.70.Dd, 64.70.pv, 83.10.Mj, 83.80.Hj

The fundamental understanding of the relation between microscopic structure, dynamics, and flow properties in complex yield stress materials is a challenging and open problem with widespread applications in metals, plastics, paints, slurries, etc. [1]. The glassy state, ubiquitous in natural, biological, and synthetic systems, also poses a frontier question in condensed matter physics. Colloidal glasses, associated with both phenomena, have received a lot of attention as model systems that may shed light on the glass transition and the flow of complex materials. Above a certain volume fraction, hard spheres (HS) form glasses characterized by a suppressed long-time diffusion [2,3] and a yield stress behavior [4]. Steady and oscillatory shear experiments show that, beyond a critical yield strain, they flow due to shear-induced cage breaking and irreversible out-of-cage particle rearrangements [5,6] with the stress and the structural relaxation rate increasing sublinearly with the shear rate [4,7], while slip and shear banding phenomena are detected at low rates [8,9]. Although the vast majority of studies investigate steady shear, the transient response encompasses the underlying mechanisms for shear melting and may provide insight on the glass state at rest. Step rate experiments and simulations performed on systems such as polymers [10], nanocomposites [11], metallic glasses [12], soft colloids [13], and colloidal gels [14] show an initial stress increase, often followed by a stress overshoot before the steady state is reached. For HS suspensions, mode coupling theory, molecular dynamics simulations, and confocal microscopy [15,16] indicate a relation of the stress overshoot with a superdiffusive particle motion attributed to negative correlations in the stress autocorrelation function. Beyond the mean-field-type approach of mode-coupling theory [17], however, a complete understanding linking the local microscopic structure and particle displacements at the level of the cage with macroscopic rheology during yielding is still lacking.

Here, we investigate the start-up flow of model HS glasses and supercooled liquids using rheology, confocal microscopy, and Brownian dynamics (BD) simulations in order to elucidate the yielding mechanisms during start-up shear at the particle level. We find that the stress overshoot marking the transition from an elastic deformation to a steady-state plastic or viscous flow is linked to cage deformation, which increases with shear rate and decreases approaching random close packing. The evolution of structural anisotropy is manifested mainly by a decrease of the maximum of the pair-distribution function in the extension axis. Such a microstructural response leads to a decrease of the short-time diffusion due to cage constriction and to superdiffusive displacements at the crossover between in-cage and shear-induced out-of-cage motion.

We used sterically stabilized poly(methyl methacrylate) (PMMA) model hard-sphere particles with radius $R = 267$ nm ($\sim 6\%$ polydispersity) suspended in decalin for rheology. Confocal microscopy requires larger particles; we utilized fluorescent PMMA particles with $R = 788$ nm ($\sim 6\%$ polydispersity) in a density matching *cis*-decalin–bromocycloheptane mixture with 4 mM tetrabutylammoniumchloride salt to screen the weak charges present in the mixture [15]. We prepared different volume fractions by progressively diluting a single batch with the volume fraction determined in the coexistence regime or from random close packing [2]. Step rate tests were conducted on an Anton-Paar MCR501 rheometer with cone-plate geometry (25 and 50 mm diameter and 0.01 rad angle) using a solvent trap to minimize evaporation. Confocal microscopy under shear utilized a piezoelectrically driven homemade parallel plate shear cell in conjunction with a fast scanning confocal unit (VTeye, Visitech) mounted on an inverted microscope (Nikon) [15]. We also performed BD simulations where HS interactions were implemented through the potential free algorithm [18], allowing direct comparison

with experiments both in terms of interactions and volume fractions. Affine shear was applied on typically 5405 particles with a polydispersity of 10% and periodic boundary conditions.

We performed start-up shear measurements for several shear rates, $\dot{\gamma}$, at different volume fractions, ϕ. Figure 1(a) shows rheological data for the stress, σ, measured for $\phi = 0.587$ at four different $\dot{\gamma}$. After an initial sublinear increase with time, t (or strain $\gamma = \dot{\gamma}t$), due to the finite viscous contribution (nonzero G'') dissipating energy, the stress reaches a maximum, σ_{pk}, at a strain, γ_{pk}, and then decays to a steady-state value, σ_{st}. The peak stress and the magnitude of the overshoot, quantified by $\sigma_{pk}/\sigma_{st} - 1$, increase with shear rate for all volume fractions.

We quantify the interplay of shear-induced structural distortion and Brownian relaxation using the scaled Peclet number [19], $\mathrm{Pe} = \dot{\gamma}R^2/D(\phi)$, with $D(\phi)$ the ϕ-dependent short-time self-diffusion coefficient [2] taken from Stokesian dynamics simulations [20]. The bare Peclet number, $\mathrm{Pe}_0 = \dot{\gamma}t_B = \dot{\gamma}R^2/D_0$, based on the Brownian time, t_B, and the free diffusion coefficient, $D_0 = k_BT/6\pi\eta R$, is about 10 times smaller. As the shear rate increases, the stress overshoot becomes more pronounced, as Brownian motion can not fully relax the distorted structure, and the ability to store stress is increased. For the same reason, γ_{pk} increases with Pe for all ϕ [inset of Fig. 1(a)], as the cage is deformed before yielding more at larger rates. Furthermore, the magnitude of the stress overshoot decreases with increasing volume fraction [Fig. 1(b) and inset]. This reflects the fact that the available free volume decreases as random close packing is approached, minimizing the cage distortion prior to cage breaking and the ability for stress storage that will be released upon yielding, thus leading to a more brittle system.

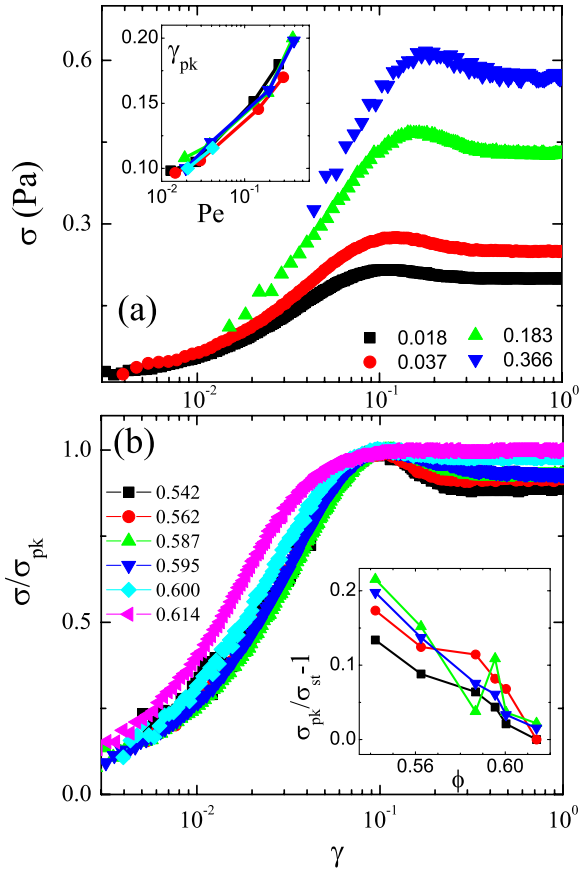

FIG. 1 (color online). (a) Stress, σ, vs strain, γ, during start-up at $\phi = 0.587$ for different scaled Pe, as indicated. Inset: Strain at the peak stress, γ_{pk}, vs Pe for the ϕ shown in (b). (b) Stress normalized by the peak stress, σ/σ_{pk}, at different ϕ, as indicated, at $\mathrm{Pe}_0 = 0.0019$ corresponding to $0.013 < \mathrm{Pe} < 0.025$. Inset: $\sigma_{pk}/\sigma_{pl} - 1$ vs ϕ for the same Pe shown in (a).

BD simulations show stress overshoots similar to the experiments, as shown in Figs. 2(a) and 2(b) for $\phi = 0.58$ and 0.62 at two Pe values. The same ϕ and $\dot{\gamma}$ dependence as in the experiments is observed, indicating that the absence of hydrodynamic interactions in BD does not play a decisive role in the range of Pe studied here (0.01–1). To understand in depth such ϕ and $\dot{\gamma}$ dependence of the stress overshoot, we turn to the microscopic structure and particle dynamics deduced both from BD simulations and confocal microscopy.

In Fig. 3, we show the projection of the pair-distribution function in the shear-gradient (xy) plane, $g_{xy}(r)$, at specific strains (A to D in Fig. 2) during start-up shear (determined for a slice of thickness $\Delta z < 0.7R$ and averaged within an

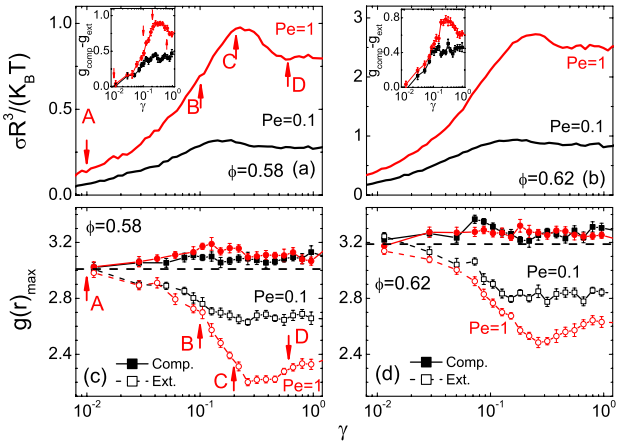

FIG. 2 (color online). BD simulations: (a),(b) Normalized transient stress for (a) $\phi = 0.58$ and (b) $\phi = 0.62$ at $\mathrm{Pe} = 0.1$ and 1, as indicated. Inset: The evolution of the difference of $g(r)_{max}$ in the compression and extension axes, g_{comp}-g_{ext}, for the two Pe of the main plot. (c),(d) Strain dependence of the maximum of $g(r)$ in the compression (solid symbols) and extension (open symbols) axes for (c) $\phi = 0.58$ and (d) $\phi = 0.62$ at $\mathrm{Pe} = 0.1$ and 1. The letters A to D indicate strains of 1%, 10%, 20%, and 60%, with the corresponding structures shown in Fig. 3. The dashed lines represent the values at rest.

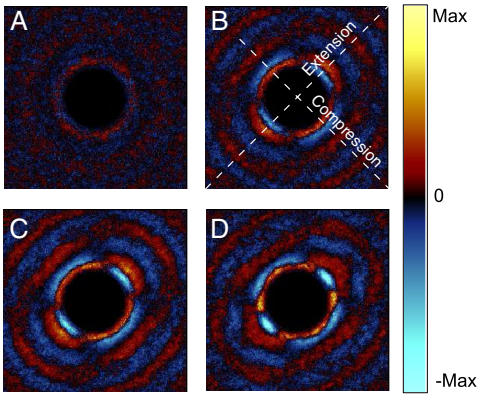

FIG. 3 (color online). BD simulations at Pe = 1 and $\phi = 0.58$: projection in the velocity-gradient (xy) plane of the difference of $g_{xy}(r)$ under shear from that at rest at different strains during start-up shear. The four images A to D correspond to the structure at 1%, 10%, 20%, and 60% strain, as indicated in Fig. 2. The density levels as compared to the system at rest are given on the right. The extension and compression axes are indicated by dashed lines.

interval of 2% strain and a bin of size $\delta r = 0.02R$) with the $g_{xy}(r)$ at rest subtracted. At point A ($\gamma = 1\%$), the structure is only slightly distorted. When the strain reaches 10% (point B), $g_{xy}(r)$ clearly indicates an increased probability to find particles at contact in the compression axis and a lower one in the extension axis. At point C ($\gamma = 20\%$), corresponding to the peak of the stress, we observe the maximum structural anisotropy with a maximally distorted cage. Beyond the stress overshoot, at the steady state (point D, $\gamma = 60\%$), $g_{xy}(r)$ exhibits more diffuse first-neighbor lobes in the extension axis that progressively are moving outwards [21]. Therefore, at the steady state, a constantly distorted cage is formed via a balance of increased particle escape along the extension axis and crowding in the compression axis [21]. Note that confocal microscopy experiments confirm such structural evolution. A measure of the structural anisotropy is the first maximum of the pair-distribution function, $g(r)_{\max}$. Since $g_{xy}(r)$ is not isotropic (Fig. 3), we determine the maxima along the compression and extension axes where the anisotropy is larger. The evolution of $g(r)_{\max}$ along these axes is shown in Figs. 2(c) and 2(d) for two volume fractions. $g(r)_{\max}$ in the compression and extension axes progressively separate as strain increases, with the former increasing and the latter decreasing below the value at rest. In the linear regime, the magnitude of the decrease of $g(r)_{\max}$ in the extension axis is the same as the increase in the compression axis. A deviation from that marks the onset of nonlinearity, at a strain of about 2–4%. However, while $g(r)_{\max}$ in compression increases only weakly with strain and reaches a plateau, on the extension axis, there is a strong decrease and a minimum around $\gamma_{\rm pk}$ (Fig. 2). The difference of $g(r)_{\max}$ in both directions [inset of Figs. 2(a) and 2(b)] closely resembles the stress evolution, indicating a direct correlation of the microstructure anisotropy with the transient macroscopic stress during yielding. The structural changes become more evident as Pe is increased but decrease with an increase of ϕ, as does the experimental stress overshoot (Fig. 1). Interestingly, although counterintuitively, both the increase of $g(r)$ at contact on the compression axis and the decrease on the extension axis contribute positively to the shear stress. This is understood by recalling that the departure from the equilibrium of the relevant deviatoric stress is [19] $\sigma_{xy} = -n^2 k_B T R(2R)^2 g^0(2R) \oint n_x n_y f d\Omega$, with n the particle number density, $g(2R) = g^0(2R)(1 + f)$, $g^0(2R)$ the value at rest, $d\Omega$ the solid angle, and n_x and n_y the components in the x and y directions of the separation vector. Hence, σ_{xy} is positive both in the compression axis where f is positive and $n_x n_y$ negative and in the extension axis where the signs of f and $n_x n_y$ are reversed.

In addition to the structure, we investigated particle dynamics under shear by confocal microscopy and BD simulations. In order to extract information for the transient microscopic dynamics, we calculated the two-time mean square displacement (MSD), $\langle \Delta r_i^2(t_w, \Delta t)\rangle = \langle [r_i(t_w + \Delta t) - r_i(t_w)]^2\rangle$ with $i = x, y, z$ (shear, gradient, and vorticity axes), as a function of $\Delta t = t - t_w$, with t_w the waiting time from the onset of shear. In this way, we monitor the evolution of the MSD for different t_w, in the initial elastic regime ($\gamma_w = \dot{\gamma} t_w = 0$), around the yield point related to the stress overshoot, and finally at the steady state. Figure 4(a) shows such two-time MSDs measured by confocal microscopy in the vorticity (z) direction for different γ_w for a supercooled liquid at $\phi = 0.56$. The MSD at rest is showing a subdiffusive regime due to the temporary caging of particles and a final out-of-cage diffusion at longer times. Here, the short-time, in-cage diffusion is not accessible by confocal microscopy due to scanning speed limits. After the onset of shear, the MSD follows the quiescent curve until a strain of a few percent is reached, where it deviates upwards, increasing stronger than linearly as it approaches the steady-state curve. This defines a transient superdiffusive behavior, as seen before [15]. As yielding is approached and cages start to break, particles temporarily move almost ballistically as they are pushed out of their cage by shear. With increasing t_w, the MSD approaches the steady-state curve and the transient superdiffusion becomes less pronounced.

In agreement with the confocal microscopy data, BD simulations show that the MSD in the vorticity direction (z) [Fig. 4(b)] at $\phi = 0.58$ exhibits a transient superdiffusion for $\gamma_w = 0$. BD at different Pe suggests that such transient behavior is more evident at Pe where the long-time shear-induced diffusion is clearly separated from the long-time diffusion at rest [Fig. 4(b)]. Furthermore, BD can also capture the short-time in-cage dynamics under shear that could not be attained by confocal microscopy or previous molecular dynamics simulations [16]. Although hydrodynamic interactions are ignored, an intriguing slowing-down

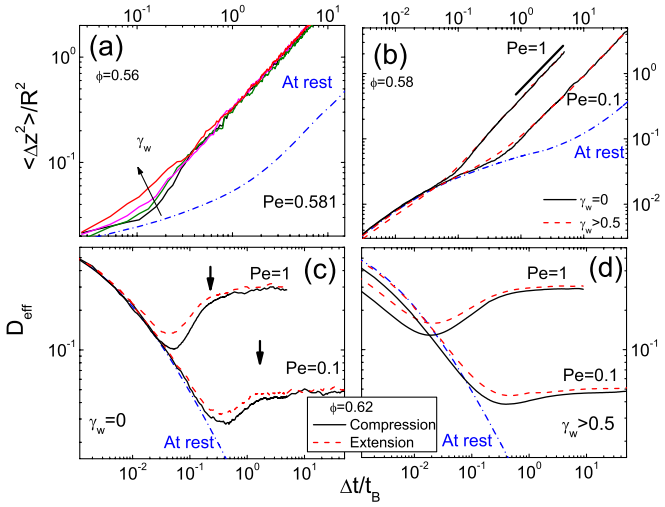

FIG. 4 (color online). Normalized MSDs under shear [(a) solid lines; (b) as indicated] and at rest [dot-dashed (blue) line] from (a) confocal data in the vorticity (z) direction for $\phi = 0.56$ and Pe $= 0.581$ at different waiting times t_w, with γ_w from 0 to 0.38 as indicated by the arrow. (b) BD simulations in the vorticity (z) direction at $\phi = 0.58$ for two different Pe in the transient ($\gamma_w = 0$) and steady-state ($\gamma_w > 0.5$) regime. (c),(d) Effective diffusion coefficients, D_{eff} (in units of t_B/R^2), from BD simulations for two Pe (0.1 and 1) in the compression and extension axes for (c) $\gamma_w = 0$ and (d) $\gamma_w > 0.5$. The arrows indicate the positions of the stress overshoot, γ_{pk} [Fig. 2(b)].

of the in-cage dynamics during fully developed shear ($\gamma_w > 0.5$) is revealed at Pe $= 1$, compared to the dynamics at rest [Fig. 4(b)]. This finding indicates that shear-induced structural changes affect in-cage dynamics. As shown in Figs. 2 and 3, the cages are continuously deformed in a flowing HS glass, with their dimensions shrunk in the compression and elongated in the extension axis. Such constriction leads to a slower in-cage diffusion.

The slow-down of the short-time diffusion and the superdiffusive behavior are better seen by plotting an effective diffusivity $D_{\text{eff}} = \langle \Delta r_i^2(t_w, \Delta t)\rangle/2\Delta t$ (or average slope of MSD), as shown in Figs. 4(c) and 4(d) for the transient regime ($\gamma_w = 0$) and the steady state, respectively. We may follow D_{eff} from MSDs projected in the compression and extension axis, where the most pronounced structural changes are detected (Fig. 3). In Fig. 4(c), D_{eff}, determined immediately after shear is imposed ($\gamma_w = 0$), drops from its zero-strain value at rest to that at long times, which corresponds to the steady-state value, passing through a minimum. The minimum of D_{eff} occurs well before the stress overshoot (at γ_{pk}) and the minimum of $g(r)_{\text{max}}$ in the extension axis [see Figs. 2(b) and 4(c), and [21]). In the early elastic regime, D_{eff} follows the quiescent curve, since the cage is not yet deformed and in-cage diffusion is still unaffected. At larger strains, though, the superdiffusive transition from in-cage to out-of-cage particle motion is strongly pronounced on the compression axis where particle density is enhanced. One might expect the absence of any superdiffusion at the steady state for a high $\dot{\gamma}$ where the shear-induced in- and out-of-cage diffusion are equal. However, BD shows that this is not the case. In Fig. 4(d), we show D_{eff} in the compression and extension axes measured in the steady state following yielding ($\gamma_w > 0.5$). At high rates (Pe $=$ 1), a superdiffusive response is detected at time scales separating short-time in-cage and long-time out-of-cage shear-induced motion [Fig. 4(b)]. This is an important finding, suggesting that, even at the steady state, there still exists a dynamic signature of particle caging that shows up as a continuous breakdown and reformation of the cage. A similar response is detected in the velocity and gradient directions (not shown) after subtracting the affine motion due to shear.

In Fig. 4(d), the slowing-down of the short-time in-cage diffusion due to cage deformation is clearly manifested as a drop of D_{eff} at short times (or strains) compared to the values at rest and is stronger at higher ϕ. It is noteworthy that such a slowing-down is more pronounced in the compression axis and weaker in the extension axis [Fig. 4(d)], in support of our interpretation that particles under shear are pushed together in the compression axis, creating a denser cage while they diffuse out of their cages mainly along the extension axis. Increasing Pe [Fig. 4(d)] and ϕ (not shown) enhances this behavior. A further interesting observation is that, at long times, D_{eff} [Fig. 4(d)] or the MSDs (not shown) in the compression and extension axis approach each other due to an averaging of shear-induced out-of-cage displacements of all particles moving along different directions.

In summary, we have presented a comprehensive study of yielding of concentrated hard-sphere suspensions and glasses during start-up shear combining rheology, confocal microscopy, and BD simulations. The detailed relation between structure, dynamics, and stress is revealed. Under shear, the cage starts to be deformed in the initial elastic regime and structural anisotropy progressively builds up, mainly affecting $g(r)$ at contact in the extension axis that shows a minimum at a strain where the stress overshoot is observed. Both become stronger with increasing rate and decrease as volume fraction is increased, linking structural cage deformation and stress response. At a fixed volume fraction, the Peclet number determines the degree of microstructural anisotropy and the magnitude of the overshoot: At the limit of low Pe, no overshoot is observed, since stress is completely relaxed through Brownian diffusion before the cage is considerably distorted, whereas, at high Pe, cage deformation is rapid enough that stress can be stored before yielding and relaxes partly at the steady state. At fixed Pe, the ϕ dependence is governed by the available free volume: At high ϕ, approaching random close packing, the stress overshoot decreases, since no large deformation and stress storage is

possible due to the restricted free volume before the cage breaks.

The microstructural anisotropy and the stress overshoot are related to the transient superdiffusion detected at the transition from rest to steady shear flow. While the Pe dependence of the two phenomena is comparable, the ϕ dependence is different, suggesting that the two phenomena are not linked to exactly the same mechanism. More importantly, though, a superdiffusive response is revealed for the first time at the steady state, marking the transition from in-cage to out-of-cage motion at high shear rates. This provides clear evidence of the dynamic character of cages that continuously break and reform under shear. Furthermore, at short times, cage deformation restricts local motions, particularly in the compression axis, leading to an overall slowing-down of in-cage diffusion.

The detailed microscopic mechanisms of yielding probed here in model hard-sphere glasses may be used as guidelines to further understand other complex soft matter systems with more complicated interparticle interactions.

We thank A. B. Schofield for the colloids and K. J. Mutch for stimulating discussions. We acknowledge funding from EU Marie-Curie ToK "Cosines," NoE "SoftComp," and NMP Small "Nanodirect"; the Greek GSRT (ΠΕΝΕΔ-03ΕΔ); and the Deutsche Forschungsgemeinschaft (DFG) within SFB-TR6.

*georgp@iesl.forth.gr

[1] R. G. Larson, *The Structure and Rheology of Complex Fluids* (Oxford University Press, New York, 1999).

[2] P. N. Pusey, in *Liquids, Freezing, and the Glass Transition*, Proceedings of the Les Houches Summer School, Session L1, edited by J. P. Hansen, D. Levesque, and J. Zinn-Justin (Elsevier, Amsterdam, 1991).

[3] G. Brambilla, D. El Masri, M. Pierno, L. Berthier, L. Cipelletti, G. Petekidis, and A. B. Schofield, Phys. Rev. Lett. **102**, 085703 (2009).

[4] G. Petekidis, D. Vlassopoulos, and P. N. Pusey, J. Phys. Condens. Matter **16**, S3955 (2004).

[5] G. Petekidis, A. Moussaïd, and P. N. Pusey, Phys. Rev. E **66**, 051402 (2002).

[6] G. Petekidis, D. Vlassopoulos, and P. N. Pusey, Faraday Discuss. **123**, 287 (2003).

[7] R. Besseling, E. R. Weeks, A. B. Schofield, and W. C. K. Poon, Phys. Rev. Lett. **99**, 028301 (2007).

[8] P. Ballesta, R. Besseling, L. Isa, G. Petekidis, and W. C. K. Poon, Phys. Rev. Lett. **101**, 258301 (2008).

[9] R. Besseling, L. Isa, P. Ballesta, G. Petekidis, M. E. Cates, and W. C. K. Poon, Phys. Rev. Lett. **105**, 268301 (2010).

[10] Y. Wang and S-Q. Wang, J. Rheol. **53**, 1389 (2009).

[11] W. Letwimolnun, B. Vergnes, G. Ausias, and P. J. Carreau, J. Non-Newtonian Fluid Mech. **141**, 167 (2007).

[12] M. L. Falk, J. S. Langer, and L. Pechenik, Phys. Rev. E **70**, 011507 (2004).

[13] V. Carrier and G. Petekidis, J. Rheol. **53**, 245 (2009); S. Rogers *et al.*, *ibid.* **54**, 133 (2010).

[14] N. Koumakis and G. Petekidis, Soft Matter **7**, 2456 (2011); M. Laurati *et al.*, J. Rheol. **55**, 673 (2011).

[15] J. Zausch, J. Horbach, M. Laurati, S. U. Egelhaaf, J. M. Brader, Th. Voigtmann, and M. Fuchs, J. Phys. Condens. Matter **20**, 404210 (2008).

[16] J. Zausch and J. Horbach, Europhys. Lett. **88**, 60 001 (2009).

[17] J. M. Brader, Th. Voigtmann, M. Fuchs, R. G. Larson, and M. E. Cates, Proc. Natl. Acad. Sci. U.S.A. **106**, 15 186 (2009).

[18] R. Foss and J. F. Brady, J. Rheol. **44**, 629 (2000).

[19] J. F. Brady, J. Chem. Phys. **99**, 567 (1993).

[20] A. Sierou and J. F. Brady, J. Fluid Mech. **448**, 115 (2001).

[21] See Supplemental Material at http://link.aps.org/supplemental/10.1103/PhysRevLett.108.098303 for a video that shows the structural and stress evolution during start-up.